



# Motility and Segregation of Hsp104-Associated Protein Aggregates in Budding Yeast

Chuankai Zhou,<sup>1,2</sup> Brian D. Slaughter,<sup>1</sup> Jay R. Unruh,<sup>1</sup> Amr Eldakak,<sup>1</sup> Boris Rubinstein,<sup>1</sup> and Rong Li<sup>1,2,\*</sup>

<sup>1</sup>Stowers Institute for Medical Research, 1000 East 50th Street, Kansas City, MO 64110, USA

<sup>2</sup>Department of Molecular and Integrative Physiology, University of Kansas Medical Center, 3901 Rainbow Boulevard, Kansas City, KS 66160, USA

\*Correspondence: [rli@stowers.org](mailto:rli@stowers.org)

DOI 10.1016/j.cell.2011.11.002

## SUMMARY

During yeast cell division, aggregates of damaged proteins are segregated asymmetrically between the bud and the mother. It is thought that protein aggregates are cleared from the bud via actin cable-based retrograde transport toward the mother and that Bni1p formin regulates this transport. Here, we examined the dynamics of Hsp104-associated protein aggregates by video microscopy, particle tracking, and image correlation analysis. We show that protein aggregates undergo random walk without directional bias. Clearance of heat-induced aggregates from the bud does not depend on formin proteins but occurs mostly through dissolution via Hsp104p chaperon. Aggregates formed naturally in aged cells also exhibit random walk but do not dissolve during observation. Although our data do not disagree with a role for actin or cell polarity in aggregate segregation, modeling suggests that their asymmetric inheritance can be a predictable outcome of aggregates' slow diffusion and the geometry of yeast cells.

## INTRODUCTION

Budding yeast cells divide asymmetrically to generate a new cell with full proliferative potential and an aging mother cell that can be anywhere along a finite replicative life span (20–30 cell divisions under standard laboratory conditions) (Mortimer and Johnston, 1959). This asymmetry in replicative age is correlated with an unequal segregation of aging determinants along the axis of cell polarity in a dividing yeast cell (Egilmez and Jazwinski, 1989; Sinclair and Guarente, 1997). One class of such aging determinants is aggregates formed by damaged proteins. A seminal study demonstrated that aggregates containing carbonylated proteins, which result from oxidative damage in aging cells, are preferentially retained by the mother during bud formation and cell division (Aguilaniu et al., 2003). Such asymmetric segregation of damaged proteins appears to be

dependent on the actin cytoskeleton (Aguilaniu et al., 2003; Knorre et al., 2010; Tessarz et al., 2009). However, the mechanism by which actin regulates asymmetric partitioning of protein aggregates remains elusive.

In a recent study (Liu et al., 2010), segregation of protein aggregates was studied using a model system in which heat-induced protein aggregates were labeled with GFP-tagged Hsp104p, a hexameric AAA ATPase-based chaperon known to play a major role in the modification and dissolution of heat-denatured protein aggregates (Parsell et al., 1994; Glover and Lindquist, 1998; Bösl et al., 2006; Doyle and Wickner, 2009). This study implicated several proteins that control the assembly of actin cables, most notably the formin family actin-nucleating protein Bni1p, in the segregation of Hsp104-containing protein aggregates. Actin cables are parallel bundles of actin filaments (F-actin), best known for their role in polarized trafficking of membrane and cell wall materials and organelles during polarized growth (Pruyne et al., 2004). During the early stage of bud growth, actin cables are nucleated from Bni1p localized at the tip of the nascent bud (Evangelista et al., 2002; Sagot et al., 2002). Elongation of actin filaments at their barbed ends generates a retrograde flow of actin subunits in the mother-bound direction (Yang and Pon, 2002). It was proposed that the Hsp104p-containing protein aggregates associate with actin cables, possibly through a direct interaction of Hsp104p with actin, and ride along the retrograde flow to clear from the bud prior to cell division (Liu et al., 2010). Supporting this model, time-lapse movies were presented showing movement of single aggregates in the bud across the bud neck into the mother compartment.

A polarized array of actin cables exists during the part of the cell cycle when the cell undergoes rapid polarized growth, but after mitotic entry, the actin organization becomes isotropic (Adams and Pringle, 1984; Lew and Reed, 1995; Pruyn and Bretscher, 2000). Thus, an initial question motivating our study was how mitotic cells might rely on the actin retrograde flow to clear protein aggregates from the bud prior to cytokinesis. We used live imaging to observe the dynamics and movement of Hsp104p-containing protein aggregates. Surprisingly, we found a lack of defined directionality in aggregate movement during budding or other cell-cycle stages. Instead, heat-induced aggregates exhibit random walk and are largely cleared from

the bud via Hsp104p ATPase-dependent dissolution. Interestingly, whereas actin depolymerization reduced aggregate random movement and the rate of dissolution, formin proteins do not play any detectable positive role in these events. Based on these findings, we propose an alternative model to explain the asymmetric inheritance of protein aggregates during yeast asymmetric cell division.

## RESULTS

### Heat-Induced Protein Aggregates Undergo Random Walk

We used the same approach as described (Liu et al., 2010) to observe the dynamics of protein aggregates in live yeast cells. In brief, protein aggregates were induced with a short (30 min) heat shock at 42°C and visualized with Hsp104-GFP. As in Liu et al., we used the *HSP104-GFP* strain from the yeast genome-wide GFP-tagged strain collection (Huh et al., 2003), in which GFP was introduced at the 3' end of the *HSP104* open reading frame in the genome of the S288c strain BY4741. After a brief recovery at 30°C following the heat shock, the cells were imaged by acquiring three-dimensional (3D) time-lapse confocal movies (see [Experimental Procedures](#)). As shown in [Figure 1A](#) and [Movie S1](#) available online, the majority of protein aggregates were motile in both the mother and the bud at all cell-cycle stages. Most aggregate movements were confined within the bud or the mother, but bud-to-mother ( $B > M$ ) or mother-to-bud ( $M > B$ ) translocation of the aggregates could be observed at low frequencies with a slight bias in the  $M > B$  direction ([Figures 1B–1E](#) and [Movies S2A](#) and [S2B](#)). Quantification of  $B > M$  and  $M > B$  movements in small-budded cells (bud diameter equal to or less than 1/3 of that of mother, indicating the stage of polarized growth) revealed no directional bias in aggregate motility ([Figures 1F](#) and [1G](#)).

To quantitatively characterize aggregate movement, we performed automated tracking of individual aggregates ([Experimental Procedures](#)) ([Figure 2A](#), left, and [Movie S3](#)). The mean square displacement (MSD) averaged from 1,068 traces showed that the aggregate movement can be approximated as random walk with a small amount of confinement ([Figure 2B](#)). For pure random walk (diffusion), one expects a linear relationship between MSD and time shift ( $\text{MSD}(\tau) = 4D\tau^\alpha$ , wherein  $\alpha = 1$ ), whereas confinement (subdiffusion) results in a downward trending relationship ( $\alpha < 1$ ) and transport (superdiffusion) results in an upward trending relationship ( $\alpha > 1$ ). Simulations of random walk based on the observed trajectory lengths showed overall similar trajectory profiles as those observed experimentally, including the occasional more linear trajectories ([Figure 2A](#), right, compared to left). As it is possible that a small fraction of transport (or superdiffusion) may be obscured by averaging, we performed 5,000 simulations of aggregate movement, with the diffusion coefficient and trajectory length distribution similar to those observed in yeast cells for three scenarios: (1) pure random walk; (2) random walk with 10% superdiffusion; and (3) random walk with 30% subdiffusion. The distribution of  $\alpha$  values for each population was compared to the experimentally observed distributions ([Figure 2C](#)). This analysis found that the experimentally observed distribution matches the shape of

the predicted distribution from scenario (3), indicating that the experimental data are consistent with a model that does not include transport. Quantification of  $\alpha$  values in small-budded cells showed that the mode of aggregate motility at this cell-cycle stage is indistinguishable from that of the entire population ([Figure 2D](#)).

To ensure that the Hsp104-GFP-expressing strain in our collection had not accumulated random mutations that might disrupt the normal behavior of protein aggregates, we obtained and tested the Hsp104-GFP strain used in the previous work (Liu et al., 2010). This strain showed the same aggregate behavior as our Hsp104-GFP strain ([Movie S4](#) and [Figures 3A](#) and [3B](#)). We also reconstructed a new Hsp104-GFP strain by genomic tagging of *HSP104* in the BY4741 parental wild-type strain. Observation of protein aggregate movement using this strain was again consistent with the above two strains (data not shown).

### Hsp104p Chaperon-Mediated Dissolution Is the Main Mechanism of Heat-Induced Aggregate Clearance

Aside from the random motion of the protein aggregates described above, another apparent behavior of the aggregates is their dissolution: during the initial segment of the movies (up to ~20 min), the aggregates grew slightly brighter but then underwent gradual reduction in brightness and number during the rest of the 1–1.5 hr movies ([Figure 4A](#), arrow, and [Movie S5](#)). Near the end of the movies, most buds, which had fewer aggregates initially, were cleared of aggregates by this means, whereas the mothers had drastically reduced number of aggregates compared to the initial amounts. By acquiring serial confocal slices spanning the entire Z dimension of cells in these movies, we could rule out the possibility that aggregate disappearance was due to movement out of the focal plane. Concomitant with aggregate dissolution, the diffuse cytosolic GFP level rose likely as a result of release of free Hsp104-GFP ([Figure 4A](#)). This observation is consistent with the previously reported role for Hsp104 in dissolving heat-induced aggregates (Parsell et al., 1994; Glover and Lindquist, 1998; Bösl et al., 2006; Doyle and Wickner, 2009).

To evaluate the contribution of dissolution to aggregate clearance from the bud relative to that from  $B > M$  movement, we quantified the likelihood of these events from the time-lapse movies. As shown in [Figure 4B](#), in ~96% of the cells observed, aggregate clearance (defined as disappearance of the last aggregate) from the bud occurred via dissolution (white bar), whereas only ~4% of cells lost their last aggregate by  $B > M$  movement (gray bar). Furthermore, in nearly all cases of the latter, the observed  $B > M$  movement was a single such event per cell, before which most of the aggregates in the bud were cleared already via dissolution. As previously reported (Liu et al., 2010), we also observed fusion of colliding aggregates in both mother and the bud ([Figure 4A](#), arrowhead, and [Movie S5](#)), and large aggregates could sometimes be observed to split into smaller aggregates (data not shown).

We next tested the possibility that the observed aggregate dissolution is a result of the Hsp104p chaperon activity by using a mutation, *hsp104*<sup>Y662A</sup>, that does not affect Hsp104p binding to protein aggregates but disrupts the refolding activity

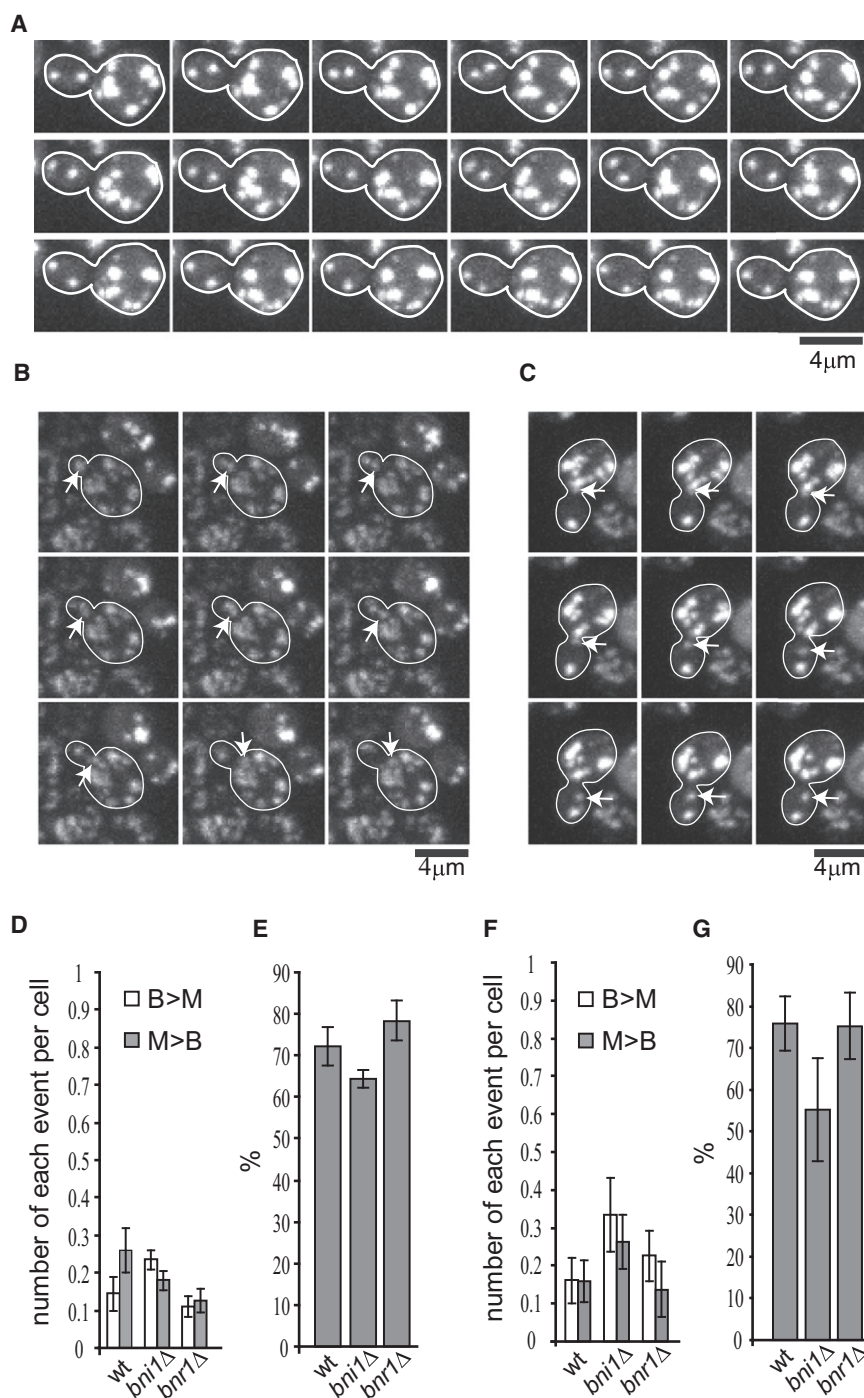


**Figure 1. Three-Dimensional Time-Lapse Imaging of Heat-Induced Hsp104p-Containing Protein Aggregates**

(A) Observation of Hsp104-GFP-containing aggregate movement in the wild-type BY4741 strain in a representative three-dimensional (3D) time-lapse movie (Movie S1A). Image stacks were collected and shown at 20 s intervals and are shown as maximum projections.

(B) Example of an aggregate (arrow) moving from bud to mother in wild-type (Movie S2A). Image stacks were collected and shown at 1 min intervals and are shown as maximum projections.

(C) Example of an aggregate (arrow) moving from mother to bud in wild-type (Movie S2B). Image stacks were collected at 1 min intervals, and a maximum projection is shown.

(D) The frequency of B > M or M > B movement per cell in a growing population was calculated by counting the total number of each type of event divided by the total number of budded cells observed in each movie. The bar graphs show mean and standard error of the mean (SEM).

(E) Percentage of cells in the population in (D) in which no *trans*-bud neck movement was observed during the 1 hr time-lapse movies. Shown are mean and SEM. For both (D) and (E), on average, 40 cells/movie from four to six movies were quantified for each strain.

(F) The frequency of B > M or M > B movement per small-budded cell was calculated by counting the total number of each type of event divided by the total number of small-budded cells observed in each movie. Shown are mean and SEM.

(G) Percentage of cells in the population in (F) in which no *trans*-bud neck movement was observed during the 1 hr time-lapse movies. Shown are mean and SEM. For (F) and (G), on average, 14 cells/movie from four to six movies were quantified for each strain.

of Hsp104p (Lum et al., 2004). A strain was constructed in which the genomic copy of *HSP104* was replaced with *hsp104<sup>Y662A</sup>-GFP*. This mutant strain exhibited more aggregates than the wild-type immediately after heat shock, and the aggregates in the mutant did not show any dissolution throughout the 3 hr time-lapse movie (Figure 4C and Movie S6A). In fact, quantification showed that the aggregates in *hsp104<sup>Y662A</sup>-GFP* strain continued to increase in their intensity (Figure 3C). This observation is consistent with the notion that the Hsp104p chaperon

activity plays a major role in protein disaggregation in yeast (Parsell et al., 1994; Glover and Lindquist, 1998; Bösl et al., 2006; Doyle and Wickner, 2009).

**Hsp104p and F-Actin, but Not Bni1p, Play a Role in the Random Movement and Dissolution of Heat-Induced Aggregates**

We observed that, in addition to a lack of dissolution, the movement of protein aggregates was largely abolished in *hsp104<sup>Y662A</sup>-GFP* cells (Movie S6A). As this reduced movement could possibly be due to overcrowding of the aggregates in the mutant cells, we performed another experiment by subjecting the mutant cells to a much shorter (3.5 min) heat shock, which results in an aggregate density similar to that in wild-type cells. In these cells, the aggregates still did not dissolve but did exhibit some motility (Movie S6B). Quantification from particle tracking data confirmed that the diffusion coefficient (D) for aggregates in the

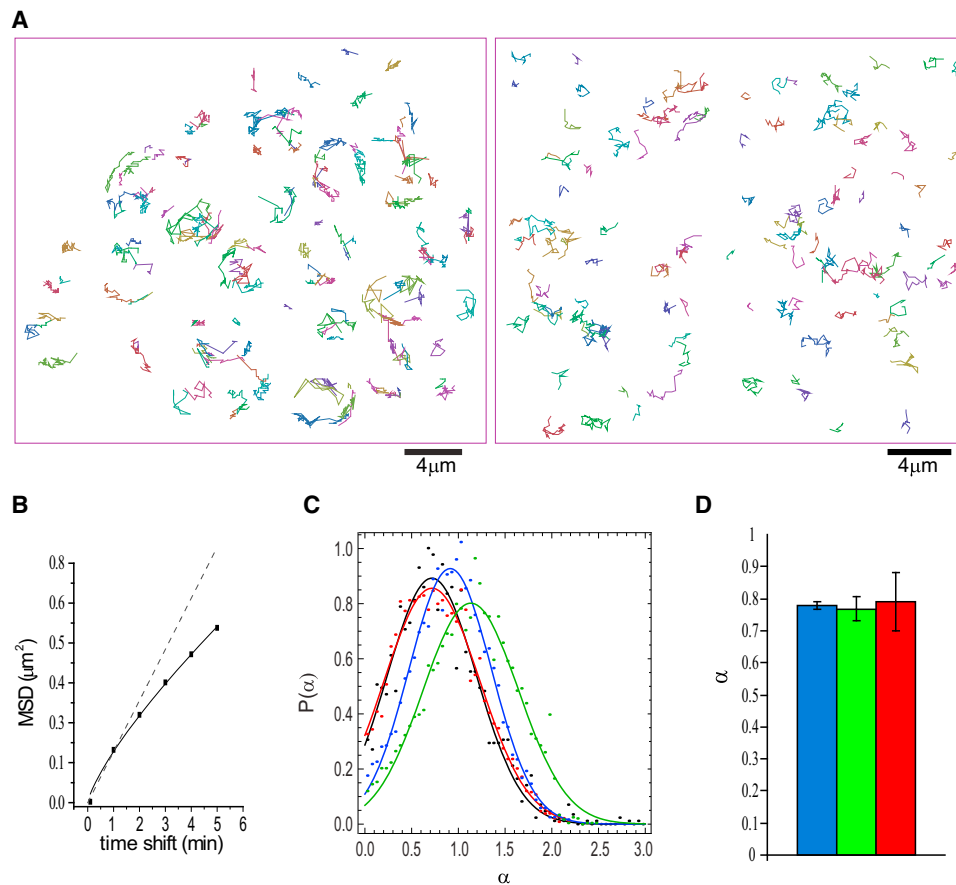


**Figure 2. Hsp104p-Containing Protein Aggregates Undergo Random Walk**

(A) (Left) A representative field of trajectories from tracking of protein aggregates from 1 hr time-lapse movies. (Right) For comparison, a field of simulated trajectories of random walk with observed distribution of trajectory lengths and diffusion coefficient.

(B) A plot of MSD versus time shift, showing that aggregate movement can be characterized as random walk with a small amount of confinement (solid line). Dotted line shows plot expected for pure random walk.

(C)  $\alpha$  value distributions from 5,000 simulations of aggregate movement with the diffusion coefficient and trajectory length distribution similar to those observed in yeast cells for each of the three scenarios: (1) pure random walk (blue); (2) random walk with 10% superdiffusion (green); (3) random walk with 30% subdiffusion (red). The distribution of  $\alpha$  values for each population was compared to the experimentally observed distribution (black), showing that the observed is consistent with scenario (3).

(D) Comparison of average  $\alpha$  values (mean and SEM) from aggregates in different population of cells in 60 min 3D time-lapse movie. (Blue) Aggregates in all of the cells in the movies ( $n = 3,542$ ); (green) all aggregates in the small-budded S/G2 cells ( $n = 182$ ); (red) aggregates in the buds of the S/G2 cells ( $n = 31$ ).  $n$  refers to the number of aggregates.

See also [Movie S3](#).

*hsp104<sup>Y662A</sup>* mutant was reduced compared to the wild-type ([Figure 3D](#)). This observation suggests that the Hsp104p ATPase activity plays a role in the movement of the aggregates. We next examined the involvement of F-actin in aggregate movement and dissolution by treating cells with latrunculin A (LatA), an inhibitor of actin polymerization. Cells were first subjected to the aforementioned protocol of 30 min heat shock and a brief recovery and then incubated with 100  $\mu$ M LatA. Time-lapse imaging started 10 min after LatA addition, at which time most of the cellular actin filaments were undetectable by fluorescent phalloidin staining ([Figure S1](#)), and the drug was present throughout the subsequent time-lapse imaging. LatA treatment significantly reduced, though did not completely abolish, the diffusion coefficient (D) of protein aggregates ([Fig-](#)

[ure 3D](#) and [Movie S7](#)). Interestingly, the rate of aggregate dissolution was also visibly reduced ([Figure 3E](#)), suggesting that actin contributes to but is not absolutely required for the movement and dissolution of heat-induced aggregates.

To examine whether formin proteins are involved in the dissolution and movement of protein aggregates, we tagged Hsp104 with GFP in the *bni1 $\Delta$*  and *bnr1 $\Delta$*  strains (BY4741 background) and performed 3D time-lapse imaging of heat-induced aggregates ([Movies S8A](#) and [S8B](#)). Neither mutant showed reduced frequency of B > M movement of aggregates ([Figure 1D](#)). In fact, we observed a slightly higher frequency of B > M movement in *bni1 $\Delta$*  compared to that in wild-type ([Figure 1D](#)). Quantification of the rates of aggregate movement and dissolution showed that neither mutant is defective in these processes ([Figures 3D](#)



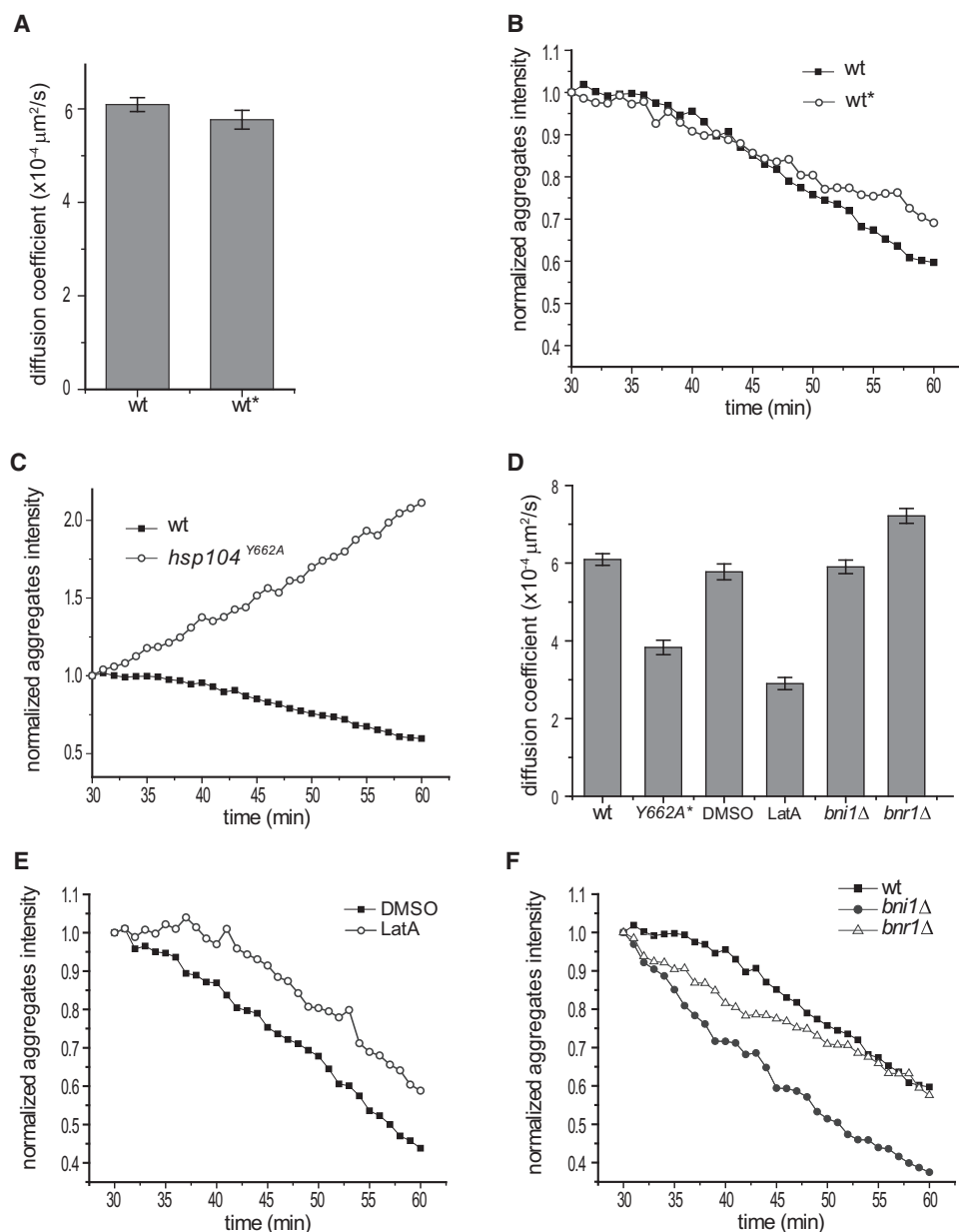


**Figure 3. Comparison of Dissolution Kinetics and Diffusion Coefficients among Different Strains and Conditions**

(A) Comparison of diffusion coefficients calculated from aggregate tracking between the two wild-type strains. Shown are mean and SEM. More than 1,000 aggregates from at least two movies/strain were tracked. WT, RLY7110; WT\*, YBD401 (Liu et al., 2010).

(B) Quantification of aggregate dissolution (see [Experimental Procedures](#)) in the two strains in (A). Shown are plots of total aggregate intensity as a function of time from time-lapse movies of a field of cells (50–100 cells per field) starting from the 30 min frame when aggregates in wild-type no longer grew in brightness. Each plot is an average from two movies. (Black square) RLY7110; (open circle) YBD401.

(C) Quantification of aggregate dissolution following the same method as in (B) in wild-type (WT) cells and *hsp104*<sup>Y662A</sup> cells.

(D) Diffusion coefficient of each strain and condition as indicated, quantified from aggregate tracking data (see [Experimental Procedures](#)). Shown are mean and SEM. \*The quantification for *hsp104*<sup>Y662A</sup> cells was done from the 3.5 min heat shock experiment to mimic wild-type aggregate density. For each strain or condition, more than 450 (and in many cases over 1,000) aggregates from two to four movies were tracked and quantified.

(E and F) Quantification of aggregate dissolution following the same method as in (B) for the same conditions or strains examined in (D).

See also Figures S1 and S2 and Movies S4, S6, S7, and S8.

and 3F). The aggregates showed slightly faster movement in *bnr1Δ* cells and faster dissolution in *bnr1Δ* than those processes in wild-type cells (Figures 3D and 3F), suggesting that Bni1 and

Bnr1 may contribute slightly negatively to aggregate dissolution or movement, respectively. Thus, the roles of F-actin in aggregate movement and dissolution appear to be largely independent of

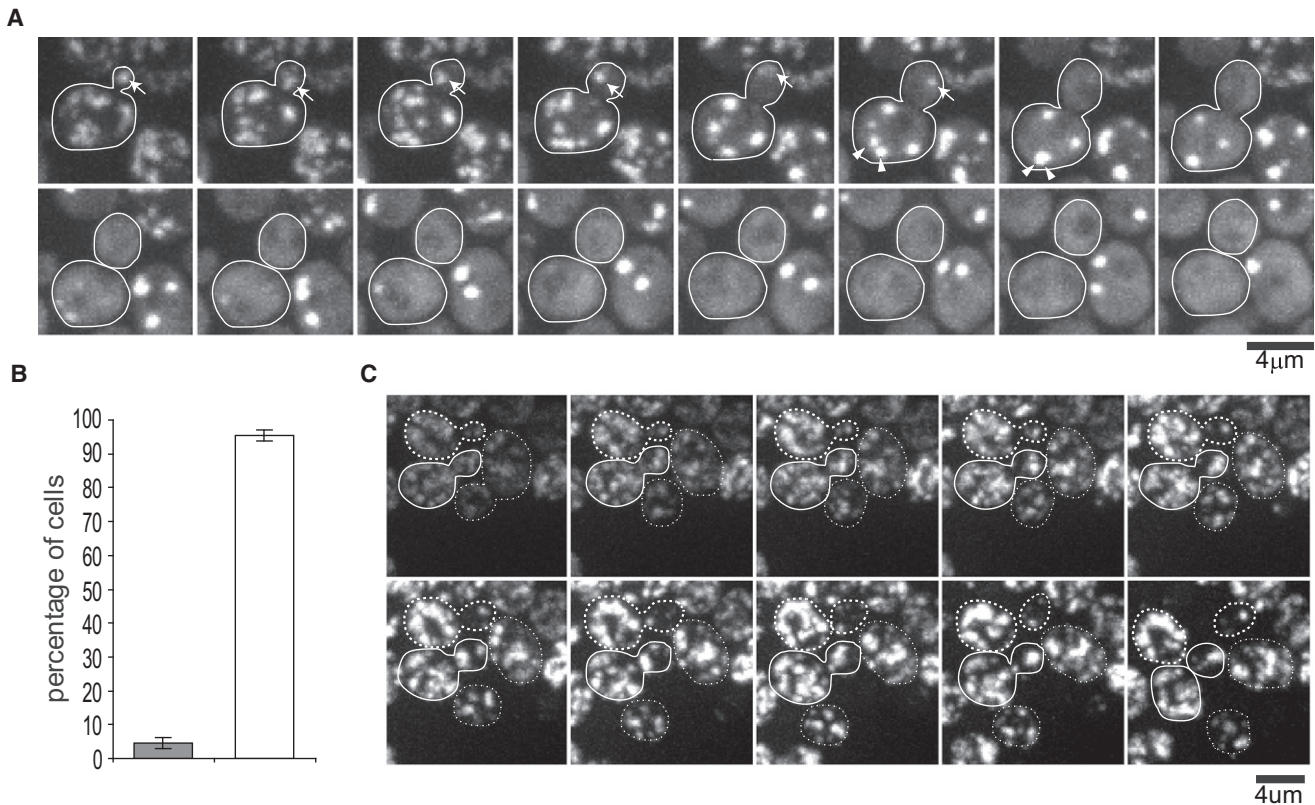


**Figure 4. Heat-Induced Aggregates Are Cleared from the Bud through Hsp104p Chaperon-Mediated Dissolution**

(A) Hsp104-GFP-associated aggregates show gradual clearance through dissolution. The arrow indicates an example of an aggregate dissolving; arrowheads indicate two aggregates fusing and then dissolving. Images stacks were collected at 1 min intervals; the montage shows maximum projections at 6 min intervals from a 90 min movie (Movie S5).

(B) Comparison of the percentage of cells in which the last aggregate was cleared from the bud by dissolution (white bar) to that by bud-to-mother movement (gray bar) in the wild-type. On average, 47 cells/movie from five movies were quantified. Shown are mean and SEM.

(C) Aggregate dissolution depends on chaperon activity of Hsp104p. In *hsp104*<sup>Y662A</sup> mutant cells, the aggregates not only did not dissolve over a representative 3 hr movie (Movie S6A), but also increased in brightness over time. Montage starts from 18 min of the movie and frames (maximum projections) are shown at 18 min intervals.

the formin proteins. We note that the calculation of aggregate diffusion coefficients in various strains or under the specified conditions was confirmed by the method of spatial temporal image correlation spectroscopy (STICS) analysis (Berland et al., 1995; Hebert et al., 2005; Kolin et al., 2006) (Figure S2), which is independent of the particle tracking approach. The rates calculated using both methods were consistent.

#### Asymmetric Inheritance of Protein Aggregates during Bud Formation

During our time-lapse confocal movies, new buds could be observed to form from a number of mother cells in each experiment. In the majority (68%) of such wild-type cells observed, the aggregates were successfully retained in the mother while the bud grew, and the new bud was devoid of aggregates throughout the movies (Figure 5A and Movie S10A). In the remainder of the population, one (two in rare cases) aggregate moved into the bud from the mother (Figure 5B and Movie S10B). In the majority of these cases, the aggregate dissolved after entry into the bud (Figures 5B and 5C and Movie S10B,

yellow arrow), whereas in a small fraction, the aggregate moved back to the mother (Figures 5B and 5C and Movie S10B, red arrow). Formin mutant (*bni1* and *bnr1*) cells undergoing budding during the time-lapse imaging essentially showed similar behavior, that is, the majority of aggregates were retained in the mother (Figure 5C and Movie S9), and those occasionally entering the bud most often dissolved (Figure 5C).

We next performed time-lapse movies to observe the dynamics and distribution of naturally accumulated Hsp104p-positive protein aggregates. Previous work showed that Hsp104p associates with protein aggregates containing carbonylated proteins resulting from oxidative damage in cells of older replicative age (Erjavec et al., 2007). In an exponentially growing population, in which most cells are young, Hsp104p-containing aggregates were rarely observed (data not shown). We hence used a magnetic beads-based sorting protocol (Chen et al., 2003) to obtain populations of wild-type enriched for older cells (see bud scar staining in Figure 6A).

The naturally formed aggregates (Figure 6B) do not dissolve during the duration of our observation by time-lapse movies,

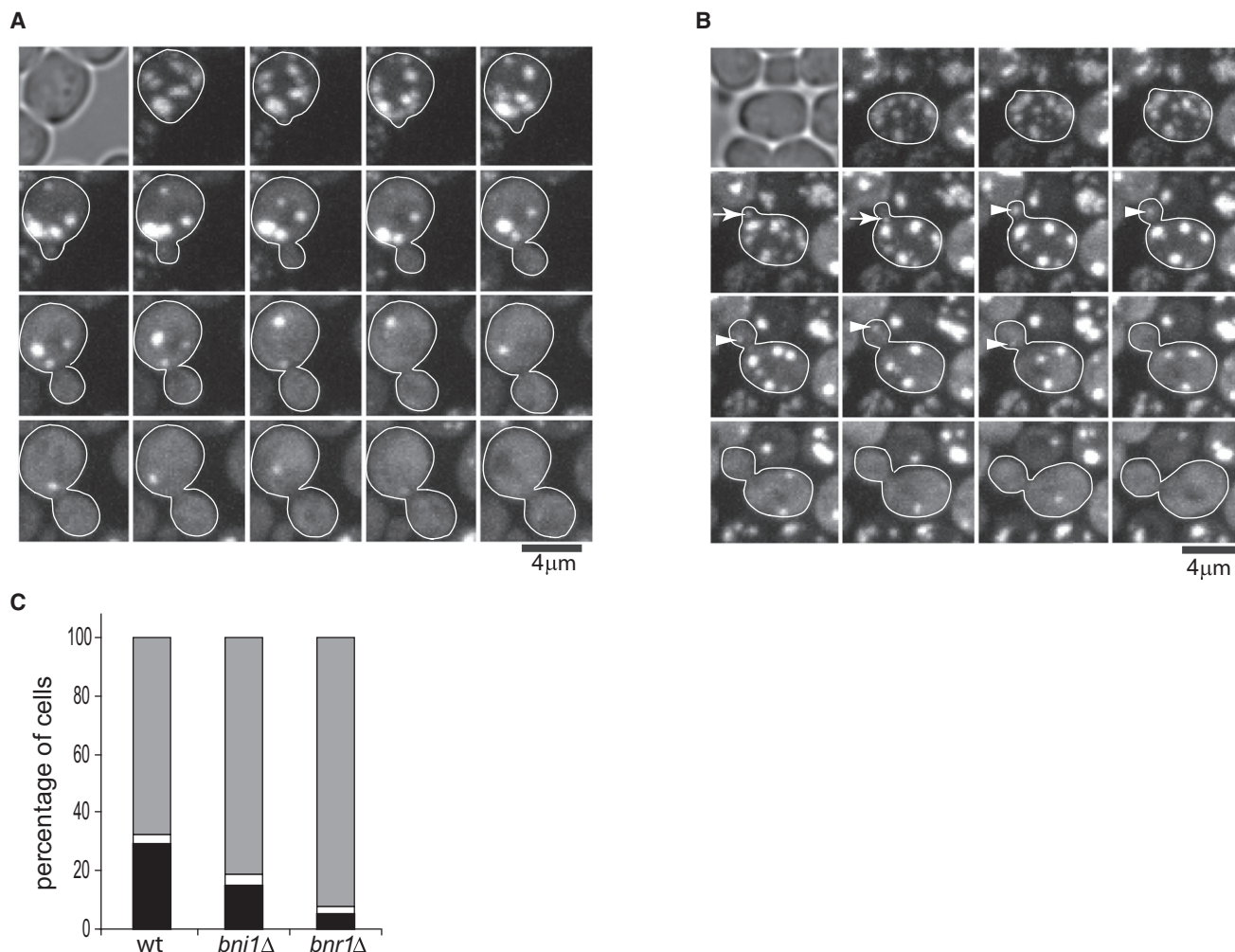


**Figure 5. Retention of Heat-Induced Protein Aggregates in the Mother during Bud Formation**

(A) An example of retention of protein aggregates in a wild-type mother cell undergoing budding. Image stacks were collected at 1 min intervals; montage is shown as maximum projections every 4 min (see also [Movie S10A](#)).

(B) Time-lapse images of a cell showing two different fates of aggregates that leaked into the bud from the mother during bud formation. Image stacks were collected at 1 min intervals; montage is shown as maximum projections every 4 min. Arrows point to an aggregate that returned to the mother after leakage into the bud; arrowhead points to an aggregate that dissolved after leakage into the bud. See [Movie S10B](#) to observe these events at a higher time resolutions.

(C) Percentages of cells displaying three different types of aggregate behavior during new bud formation and growth in three different genetic backgrounds as indicated. Cells either with a tiny bud initially devoid of any aggregates or giving birth to a new bud during the first 30 min of 1 hr long 3D time-lapse movies were scored. (Gray bar) Cells with no aggregate leakage into the bud; (black bar) cells in which aggregates leaked into the bud were subsequently cleared by dissolution; (white bar) cells in which aggregates leaked into the bud and subsequently moved back to mother.  $n = 108$  cells (WT); 74 cells (*bni1Δ*), and 133 cells (*bnr1Δ*).

See also [Movies S8](#) and [S9](#).

allowing long tracking of aggregate movement ([Figure 6C](#) and [Movie S11](#)). The individual long traces show nearly linear fitting of MSD with time, with a slight downward trend, suggesting that this movement can be described as random walk with slight confinement ([Figure 6C](#), as an example). The distributions of  $\alpha$  values from tracking many aggregates in older wild-type cells were similar to those of heat-induced aggregates ([Figure 6D](#), compared to [Figure 2C](#)). These observations suggest that the dynamics of the Hsp104-associated protein aggregates formed in different ways exhibit the same type of movement.

A recent study investigating the mechanism of asymmetric partitioning of episomal DNA circles reported free diffusive motion of episomes in the nucleoplasm ([Gehlen et al., 2011](#)). Using a numerical simulation, they demonstrated that the retention of episomes in the mother can be explained simply by the geometry of the dividing nucleus and the brief window of time in the cell cycle when nuclear division occurs. As the protein aggregates also undergo random motion, a similar explanation may be applied to the preferential retention of aggregates in the mother during cell division. To test this idea, we performed

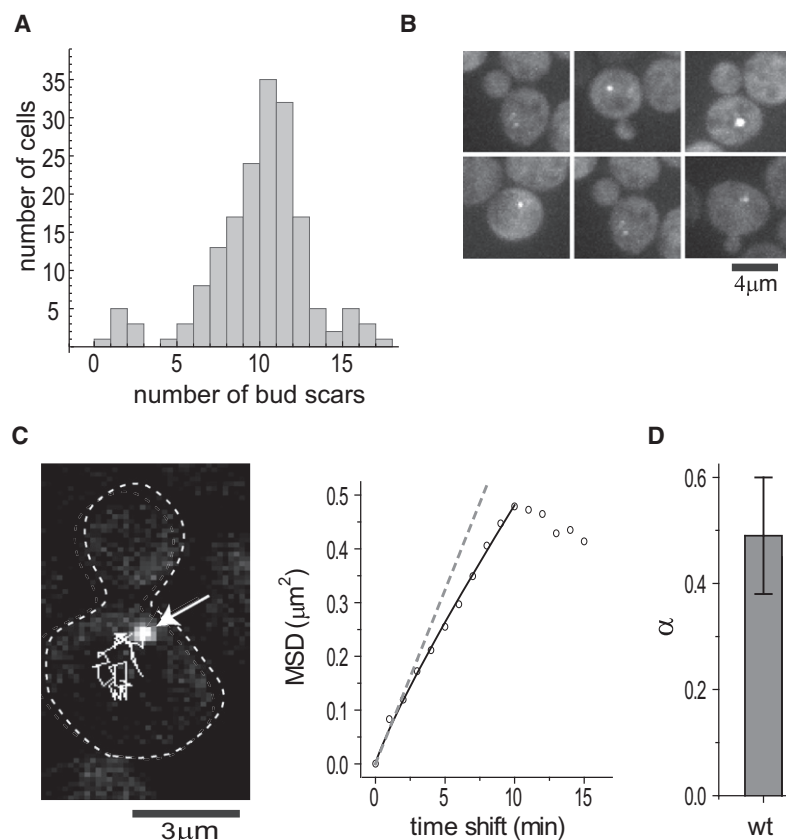


**Figure 6. Observation of Motility and Distribution of Hsp104p-Containing Aggregates in Aged Wild-Type Cells**

(A) Age distribution of magnetic beads-sorted old wild-type cells determined by bud scar counting (>170 cells were counted).

(B) Representative images showing asymmetric distribution of Hsp104-associated protein aggregates in aged wild-type from the populations in (A). Shown are maximum projections of 3D image stacks.

(C) Trajectory (white line in left) and MSD (right) analysis of an Hsp104-GFP-associated aggregate (arrow) in an old wild-type cell from a 60 min 3D time-lapse movie.

(D) Hsp104-GFP-containing protein aggregates in old wild-type cells exhibit a similar type of movement. Shown are mean and SEM of  $\alpha$  values calculated from long aggregate tracks.  $n = 21$  tracks for wild-type aggregates. See also [Movie S11](#).

a 3D numerical simulation of pure random walk, with the diffusion rate  $D = 1.0 \times 10^{-3} \mu\text{m}^2/\text{s}$  computed from particle tracking of natural Hsp104-GFP-containing aggregates in older cells. A yeast cell was represented as two spheres with radius of  $R_1 = 2.5 \mu\text{m}$  (mother) and  $R_2 = 0.85 \times R_1$  (bud) connected by a narrow neck with width  $d = 1.25 \mu\text{m}$ . Starting from an initial distribution of aggregates entirely in the mother, the probability density map after 90 min (a cell cycle) showed maintenance of a biased distribution of aggregates in the mother ([Figure 7A](#), top). To evaluate the impact of the geometry of yeast cells on this partitioning, the bud neck size was varied in the simulations. [Figure 7A](#) (bottom) shows that increasing bud neck size reduces the asymmetry in aggregate partitioning. Addition of confinement ( $\alpha = 0.50$ , approximating the average value in [Figure 6D](#)) also enhanced the segregation asymmetry as expected ([Figure 7A](#)). Aggregate asymmetric segregation can also be described using a 1D (equivalent to wide open neck) analytical model, which again shows preferential retention of aggregates in the mother even with no confinement ( $\alpha = 1$ ) ([Figures 7B and 7C](#)).

## DISCUSSION

Based on the analyses described above, we conclude that the clearance of protein aggregates from the bud does not depend on actin cable-mediated retrograde transport. Our conclusion is based on quantification of aggregates movement from time-lapse recording of a large number of cells. Although linear

bud-to-mother movement was observed occasionally, mother-to-bud movement of aggregates was observed at a similar frequency, and thus there was no net directionality in aggregate movement along the mother-bud axis. Particle tracking and trajectory analysis showed that the movement of protein aggregates can be described as random walk with a small amount of confinement. Even though some apparently linear trajectories can be observed, these can be recapitulated by random walk simulations using the same diffusion coefficient and trajectory length. We emphasize that, although our data does not support a direct role for actin-based retrograde transport in aggregate segregation, the data do not necessarily argue against an involvement for actin cytoskeleton or cell polarity proteins in this process. It is conceivable, for example, that the abnormally wide bud neck in some of the cell polarity mutants could increase the leaking of protein aggregates into the bud, although such an effect is likely to be too subtle to observe reliably in our experiments.

Disassembly of actin filaments following LatA treatment partially abrogated aggregates movement and slowed their dissolution. Although it is possible that residual actin filaments remained and were below detection in LatA-treated cells, this observation suggests that actin cables, which were no longer present in LatA-treated cells, are not required for the movement or dissolution of heat-induced aggregates. The effect of LatA on aggregate movement or dissolution may also be indirect if the loss of actin filaments induces a high-stress state interfering with aggregate dissolution or motility. Regardless of the mechanism, our observed effect of LatA on aggregate motility does not help to explain a positive role for actin in aggregate asymmetric segregation; based on our model, reduced aggregate diffusive motion would predict their better retention in the mother. The inhibitory effect of actin depolymerization on the Hsp104-dependent aggregate dissolution is consistent with a functional linkage between actin and Hsp104 reported in recent studies ([Erjavec et al., 2007](#); [Tessarz et al., 2009](#)).



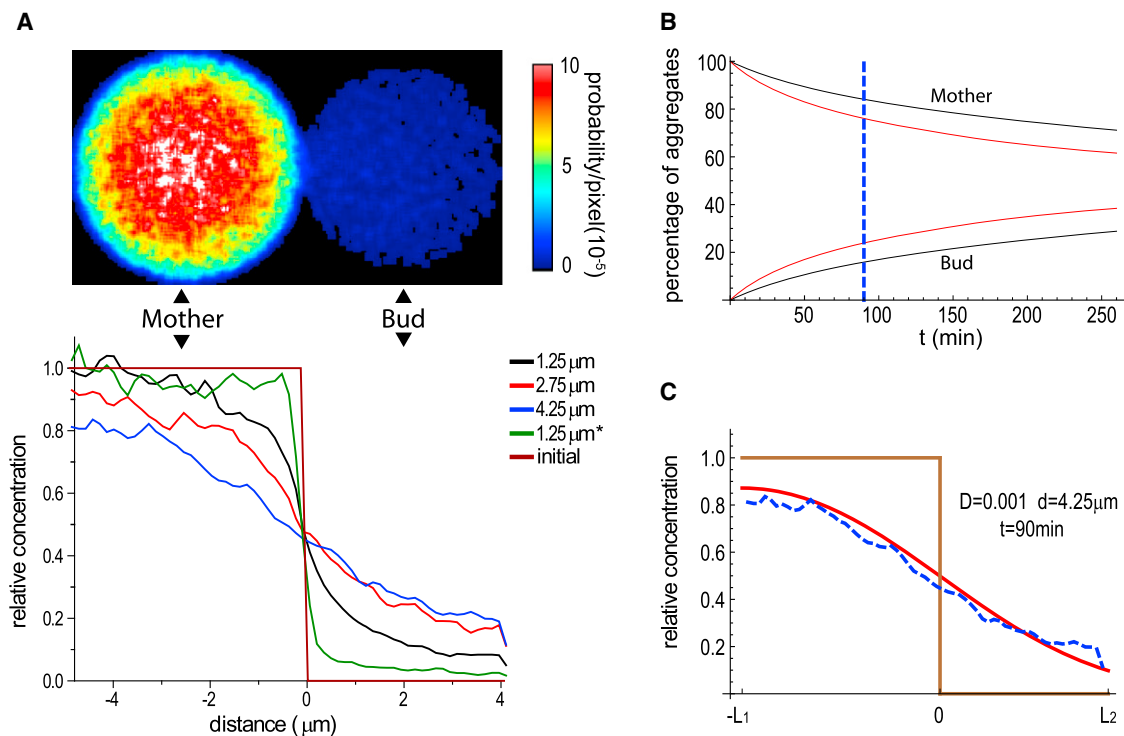


**Figure 7. Three-Dimensional Numerical Simulation and One-Dimensional Analytical Model of Aggregate Partitioning between Mother and Bud during a Yeast Cell Cycle**

(A) Probability density map of protein aggregates after a cell-cycle period (90 min) from a 3D numerical simulation of aggregate retention assuming random walk ( $\alpha = 1$ ) (see [Experimental Procedures](#)) as a 2D sum projection (top) and lateral profiles of central plane (bottom). Each colored line corresponds to simulation with a particular neck size (diameter) as indicated. The brown line shows the initial distribution at the start of the simulation, and the green line shows the 1.25  $\mu\text{m}$  neck size simulation with confined diffusion ( $\alpha = 0.50$ , as measured in aged cells).

(B) Analysis of protein aggregate retention using a 1D analytical solution (see [Equation S12](#) in [Extended Experimental Procedures](#)) for  $D = 0.0005 \mu\text{m}^2/\text{s}$  (black) and  $D = 0.001 \mu\text{m}^2/\text{s}$  (red). The dashed blue line denotes 90 min time point.

(C) A comparison of aggregate distribution after 90 min in 3D simulation for  $D = 0.001 \mu\text{m}^2/\text{s}$  and neck size of 4.25  $\mu\text{m}$  (mimicking open neck, blue dashed curve) to the 1D analytical solution (see [Equation S7](#), using 20 terms, in [Extended Experimental Procedures](#)) (red solid curve). The brown curve represents the initial aggregate distribution. 0 on x axis is the position of bud neck and mother-bud orientation as in (A); L1 and L2 are the lengths of mother and bud cell, respectively.

We did not observe any apparent requirement for the formin protein Bni1p or Bnr1p in the motility or retention of heat-induced protein aggregates in the mother. The experiments performed previously on the retention of protein aggregates relied on quantification of nonsynchronized cell populations at different time points during a continuous incubation at high temperature ([Liu et al., 2010](#)). Such an assay would not be sufficient for distinguishing between the possibilities of aggregate clearance by dissolution versus by movement. Because the dynamics of new aggregate formation during the prolonged heat exposure were unknown, buds displaying no aggregates might be new buds that formed after the cells had adapted to the heat stress and ceased the formation of new aggregates, rather than reflecting active aggregate clearance from the bud. Additionally, the unbudded cells observed in this assay might not be the new G1 cells after cytokinesis but instead might be arrested cells failing to adapt to the heat stress. By contrast, we directly observed retention of preformed aggregates during new bud formation by time-lapse movies, and we did not observe any defect in this process in the formin mutants.

Finally, based on the observed diffusion rates of protein aggregates and borrowing the insight from a recent study explaining the asymmetric inheritance of episomal DNA during yeast nuclear division ([Gehlen et al., 2011](#)), we propose that the limited mobility and the narrowness of the bud neck ensure that the vast majority of the protein aggregates accumulated with aging are retained in the mother during the limited time of a cell cycle. This idea is supported by our 3D simulation as well as a 1D analytical model. This model implies that no additional mechanism may be needed to confer the asymmetric segregation of protein aggregates during yeast cell division.

## EXPERIMENTAL PROCEDURES

### Yeast Strains

Yeast strains used in this study are based on the BY4741 S288c strain background as listed in [Table S1](#). Gene deletion or GFP tagging were performed with PCR-mediated homologous recombination ([Longtine et al., 1998](#)), and correct integrations were confirmed by PCR. To create the *hsp104<sup>Y662A</sup>-GFP* mutant (RLY7200), site-directed mutagenesis was performed by PCR using the primers described previously ([Lum et al., 2004](#)). *hsp104<sup>Y662A</sup>-GFP*

mutant DNA was sequenced, and correct integration of the mutation into the *hsp104Δ* background was confirmed by PCR. All mutant strains were analyzed by FACS and qPCR (Pavelka et al., 2010) to ensure no abnormalities in karyotype.

### 3D Fluorescence Time-Lapse Imaging of Hsp104-GFP-Containing Protein Aggregates

Yeast cells were grown in synthetic complete (SC) media containing 2% dextrose overnight at 30°C. The overnight culture was diluted to  $OD_{600} = 0.3$  and allowed to grow another 2 hr at 30°C to reach an  $OD_{600}$  of roughly 0.5. Of this midlog culture, 4 ml was transferred to 42°C for 30 min (unless indicated otherwise) and then recovered at 30°C for 10 min and 23°C for 5 min, as described in Liu et al. (2010). 1.5 ml cultures were used when heat shock was 3.5 min. The cells were placed on a thin SC (2% dextrose) agarose gel pad to allow for prolonged imaging (Tran et al., 2004). Confocal movies of Hsp104-GFP-associated aggregates were acquired using a Yokagawa CSU-10 spinning disc on the side port of a Zeiss 200 m inverted microscope. 488 nm excitation was used to excite GFP, and emission was collected through a 500–550 nm filter onto a Hamamatsu C9100-13 EMCCD. 3D image stacks were acquired every minute for 60–90 min or every 20 s for 20 min. The latter movies were performed to ensure no motility behavior was missed due to insufficient time resolution. In these movies, time-lapse recording started 20 min later than the former movies after heat shock recovery in order for better observation of aggregate movement. As we did not observe any apparent difference using two time resolutions, all data analysis presented came from movies with frames 1 min apart. Each z series was acquired with 0.5 micron step size and 15 total steps. Visual inspection confirmed that the yeast cells did not leave the focus of the z stack during the progression of the movie. Max projections were applied for each z stack to generate the final 2D data set. All image processing was performed in ImageJ software (NIH, Bethesda, MD).

### Particle Tracking and Calculation of Diffusion Coefficient

Tracking of Hsp104-GFP-associated protein aggregates was accomplished using MOSAIC ParticleTracker software (Sbalzarini and Koumoutsakos, 2005) as a plug-in to ImageJ. Prior to tracking, max projection time series were smoothened, and a rolling-background subtraction with a width of 5 pixels was applied. Inside the ParticleTracker software, a radius of 1 pixel and a percentile of 1.5% were selected (meaning the top 1.5% of most intense pixels were considered for aggregate tracking). As visual inspection verified that motion spanning 10 pixels in x or y was extremely rare, an interframe linking range of 1 and max displacement per step of 10 pixels were used. In order to calculate a MSD plot, only trajectories lasting longer than five time points were considered. The MSD was calculated using the equation  $MSD(\tau) = \langle |r(t + \tau) - r(t)|^2 \rangle$ , in Mathematica (Wolfram Research, Champaign, IL). The first five points were fit to  $MSD(\tau) = 4D\tau^\alpha$  using nonlinear least-squares fit in Mathematica. Here,  $D$  is the diffusion coefficient, and  $\alpha$  is a factor indicating nonrandom diffusion.

### Dissolution Rate Measurements

To quantitatively compare the dissolution of Hsp104-GFP-containing aggregates in various strains, it was necessary to measure the intensity of the aggregates as a function of time. All measurements were performed on background-subtracted versions of the maximum projection image for the mask creation and the sum projection image, both performed using ImageJ. A mask of the aggregates was created as follows: the maximum projection image was smoothened with a one pixel radius, followed by background subtraction using the rolling ball background subtraction ImageJ method with a radius of 5 pixels. The image was then thresholded to binary with a threshold of 10,000, and finally the binary image was dilated to ensure full coverage of the aggregates. A mask of cell areas was calculated from a smoothened maximum projection image using a threshold of 2,500. The cytoplasmic mask was calculated from the aggregates mask and the cell mask using the ImageJ xor function.

Once masks were created, they were used to calculate the average aggregates region intensity (includes cytosolic background), average cytosolic intensity, and total aggregates area. The average cytosolic intensity was subtracted

from the average aggregates region intensity to obtain the corrected average aggregates intensity without cytosolic background. Finally, the total aggregates intensity was calculated by multiplying the corrected average aggregates intensity by the aggregates area. Aggregates intensities were measured starting at 30 min after the start of acquisition because during the early part of the movies, some aggregates grew in intensity. Note that the absolute value of aggregates intensity is not important, given that they were normalized to the initial intensity for comparison between mutants or conditions.

### SUPPLEMENTAL INFORMATION

Supplemental information includes Extended Experimental Procedures, two figures, one table, and eleven movies and can be found with this article online at doi:10.1016/j.cell.2011.11.002.

### ACKNOWLEDGMENTS

The authors thank I. Pinto for assistance with yeast strain construction, J. Zhu and A. Box for help with aged cell sorting, A. Das for assistance in microscopy, and B. Liu and T. Nystrom for kindly providing their Hsp104-GFP strain. This work was supported by NIH grant RO1-GM057063 to R.L.

Received: May 4, 2011

Revised: August 3, 2011

Accepted: November 3, 2011

Published: November 23, 2011

### REFERENCES

- Adams, A.E., and Pringle, J.R. (1984). Relationship of actin and tubulin distribution to bud growth in wild-type and morphogenetic-mutant *Saccharomyces cerevisiae*. *J. Cell Biol.* 98, 934–945.
- Aguilaniu, H., Gustafsson, L., Rigoulet, M., and Nyström, T. (2003). Asymmetric inheritance of oxidatively damaged proteins during cytokinesis. *Science* 299, 1751–1753.
- Berland, K.M., So, P.T.C., and Gratton, E. (1995). Two-photon fluorescence correlation spectroscopy: method and application to the intracellular environment. *Biophys. J.* 68, 694–701.
- Bösl, B., Grimminger, V., and Walter, S. (2006). The molecular chaperone Hsp104—a molecular machine for protein disaggregation. *J. Struct. Biol.* 156, 139–148.
- Chen, C., Dewaele, S., Braeckman, B., Desmyter, L., Verstraelen, J., Borgonie, G., Vanfleteren, J., and Contreras, R. (2003). A high-throughput screening system for genes extending life-span. *Exp. Gerontol.* 38, 1051–1063.
- Doyle, S.M., and Wickner, S. (2009). Hsp104 and ClpB: protein disaggregating machines. *Trends Biochem. Sci.* 34, 40–48.
- Egilmez, N.K., and Jazwinski, S.M. (1989). Evidence for the involvement of a cytoplasmic factor in the aging of the yeast *Saccharomyces cerevisiae*. *J. Bacteriol.* 171, 37–42.
- Erjavec, N., Larsson, L., Grantham, J., and Nyström, T. (2007). Accelerated aging and failure to segregate damaged proteins in Sir2 mutants can be suppressed by overproducing the protein aggregation-remodeling factor Hsp104p. *Genes Dev.* 21, 2410–2421.
- Evangelista, M., Pruyne, D., Amberg, D.C., Boone, C., and Bretscher, A. (2002). Formins direct Arp2/3-independent actin filament assembly to polarize cell growth in yeast. *Nat. Cell Biol.* 4, 32–41.
- Gehlen, L.R., Nagai, S., Shimada, K., Meister, P., Taddei, A., and Gasser, S.M. (2011). Nuclear geometry and rapid mitosis ensure asymmetric episome segregation in yeast. *Curr. Biol.* 21, 25–33.
- Glover, J.R., and Lindquist, S. (1998). Hsp104, Hsp70, and Hsp40: a novel chaperone system that rescues previously aggregated proteins. *Cell* 94, 73–82.
- Hebert, B., Costantino, S., and Wiseman, P.W. (2005). Spatiotemporal image correlation spectroscopy (STICS) theory, verification, and application to protein velocity mapping in living CHO cells. *Biophys. J.* 88, 3601–3614.

- Huh, W.K., Falvo, J.V., Gerke, L.C., Carroll, A.S., Howson, R.W., Weissman, J.S., and O'Shea, E.K. (2003). Global analysis of protein localization in budding yeast. *Nature* 425, 686–691.
- Knorre, D.A., Kulemzina, I.A., Sorokin, M.I., Kochmak, S.A., Bocharova, N.A., Sokolov, S.S., and Severin, F.F. (2010). Sir2-dependent daughter-to-mother transport of the damaged proteins in yeast is required to prevent high stress sensitivity of the daughters. *Cell Cycle* 9, 4501–4505.
- Kolin, D.L., Ronis, D., and Wiseman, P.W. (2006). k-Space image correlation spectroscopy: a method for accurate transport measurements independent of fluorophore photophysics. *Biophys. J.* 91, 3061–3075.
- Lew, D.J., and Reed, S.I. (1995). Cell cycle control of morphogenesis in budding yeast. *Curr. Opin. Genet. Dev.* 5, 17–23.
- Liu, B., Larsson, L., Caballero, A., Hao, X., Oling, D., Grantham, J., and Nyström, T. (2010). The polarisome is required for segregation and retrograde transport of protein aggregates. *Cell* 140, 257–267.
- Longtine, M.S., McKenzie, A., III, Demarini, D.J., Shah, N.G., Wach, A., Brachat, A., Philippsen, P., and Pringle, J.R. (1998). Additional modules for versatile and economical PCR-based gene deletion and modification in *Saccharomyces cerevisiae*. *Yeast* 14, 953–961.
- Lum, R., Tkach, J.M., Vierling, E., and Glover, J.R. (2004). Evidence for an unfolding/threading mechanism for protein disaggregation by *Saccharomyces cerevisiae* Hsp104. *J. Biol. Chem.* 279, 29139–29146.
- Mortimer, R.K., and Johnston, J.R. (1959). Life span of individual yeast cells. *Nature* 183, 1751–1752.
- Parsell, D.A., Kowal, A.S., Singer, M.A., and Lindquist, S. (1994). Protein disaggregation mediated by heat-shock protein Hsp104. *Nature* 372, 475–478.
- Pavelka, N., Rancati, G., Zhu, J., Bradford, W.D., Saraf, A., Florens, L., Sander-son, B.W., Hattem, G.L., and Li, R. (2010). Aneuploidy confers quantitative proteome changes and phenotypic variation in budding yeast. *Nature* 468, 321–325.
- Pruyne, D., and Bretscher, A. (2000). Polarization of cell growth in yeast. *J. Cell Sci.* 113, 571–585.
- Pruyne, D., Legesse-Miller, A., Gao, L., Dong, Y., and Bretscher, A. (2004). Mechanisms of polarized growth and organelle segregation in yeast. *Annu. Rev. Cell Dev. Biol.* 20, 559–591.
- Sagot, I., Rodal, A.A., Moseley, J., Goode, B.L., and Pellman, D. (2002). An actin nucleation mechanism mediated by Bni1 and profilin. *Nat. Cell Biol.* 4, 626–631.
- Sbalzarini, I.F., and Koumoutsakos, P. (2005). Feature point tracking and trajectory analysis for video imaging in cell biology. *J. Struct. Biol.* 151, 182–195.
- Sinclair, D.A., and Guarente, L. (1997). Extrachromosomal rDNA circles—a cause of aging in yeast. *Cell* 91, 1033–1042.
- Tessarz, P., Schwarz, M., Mogk, A., and Bukau, B. (2009). The yeast AAA+ chaperone Hsp104 is part of a network that links the actin cytoskeleton with the inheritance of damaged proteins. *Mol. Cell. Biol.* 29, 3738–3745.
- Tran, P.T., Paoletti, A., and Chang, F. (2004). Imaging green fluorescent protein fusions in living fission yeast cells. *Methods* 33, 220–225.
- Yang, H.C., and Pon, L.A. (2002). Actin cable dynamics in budding yeast. *Proc. Natl. Acad. Sci. USA* 99, 751–756.

## EXTENDED EXPERIMENTAL PROCEDURES

### Actin Staining and LatA Treatment

Cells were fixed with 4% formaldehyde for 2 hr at room temperature with gentle shake. The cells were washed 3 times with PBS and 1 time with PBS+0.2%TX-100. Cells were resuspended in 80μl PBS+0.2%TX-100 containing 1.5μl FITC-phalloidin for 40min in dark.

In LatA experiments, mid-log cells were heat shocked and recovered as described in main text. Then 100μM LatA (Invitrogen) or the same amount of DMSO was applied to the cells for 10min. 3D time-lapse imaging was performed with present of 100μM LatA (or DMSO as control).

### Isolation of Old Cells

Cell populations with advanced replicative age were obtained by magnetic sorting (Chen et al., 2003). Exponentially growing cells were collected and washed twice with ice cold PBS (pH 8.0).  $2.5 \times 10^7$  cells were labeled with 0.5mg/ml Sulfo-NHS-LC Biotin (Pierce) at room temperature for 30 min with gentle shaking. These cells were used as M-cells. The cells were then washed twice with 1ml cold PBS to get rid of free biotin and grown in 500ml YPD for 14-15 hr ( $OD_{600}$  was not allowed to exceed 1). The separation of M-cell was carried out by incubating  $2 \times 10^9$  cells with 60μl anti-biotin microbeads (MACS) in 30ml PBS pH7.2 for 1 hr. Unbounded beads were removed by washing twice with PBS. M-cells were isolated with a magnetic sorter. Successful acquisition of cells with advanced replicative age was verified by staining of buds scars with calcaflour (main text Figure 6A).

### STICS Measurements of Particle Motion

As a second, independent method to quantify dynamics of protein aggregates, a variant of STICS and kICS was used (Berland et al., 1995; Hebert et al., 2005; Kolin et al., 2006). In STICS analysis, the spatio-temporal correlation function is measured from the raw image data as follows:

$$G(\rho, \tau) = \frac{\langle \delta I(t + \tau, r + \rho) - \delta I(t, r) \rangle_{tr}}{\langle I \rangle_{tr}^2} \quad (1)$$

Here  $\rho$  and  $\tau$  are the spatial and temporal shifts of the correlation function. This function can be quickly calculated using spatial Fourier transforms (Berland et al., 1995; Hebert et al., 2005). For randomly diffusing diffraction limited particles, the spatio-temporal correlation function is described as follows:

$$G(\rho, \tau) = G(\tau) \exp\left(\frac{-\rho^2}{\omega_0^2 + 4D\tau}\right) = G(\tau) \exp\left(\frac{-\rho^2}{\omega_0^2 + MSD(\tau)}\right) \quad (2)$$

Here the  $G(\tau)$  term is the traditional correlation function from fluorescence correlation spectroscopy and describes the amplitude of the spatial correlation, but not its spatial extent. The rest of the equation is a Gaussian function essentially identical to the spatial probability function for diffusion convolved with the microscopic point spread function (PSF). Here  $\omega_0$  is the “beam waist” of the PSF or two times the spatial standard deviation of the PSF. It is easy to see that the above equation can be extended to anomalous forms of diffusion (Schwille et al., 1999). If the spatial variance of the above equation is denoted as  $\sigma^2(\tau)$  and the variance at  $\tau = 0$  is denoted as  $\sigma^2(0)$ , then the mean squared displacement is given as:

$$MSD(\tau) = 2(\sigma^2(\tau) - \sigma^2(0)) \quad (3)$$

In order to reduce any effect of changes in Hsp104 expression level over time on the STICS map, the time series were first detrended by dividing each time point by its average. A weak threshold was applied to remove signal from the cytosol. These two processes left only aggregates and their motion as the dominating factor in the spread of the spatial cross-correlation over time. A single STICS map was calculated per 256x256 pixel field of view containing approximately between 20 and 40 cells. Each line (corresponding to each time shift) of a circular average of the STICS map was fit to a Gaussian to obtain the variance. The points at  $\rho = 0$  were not included in the Gaussian fit so as to avoid the contribution from noise and overall intensity changes. Then Equation 3 was used to determine the MSD. Similarly to the tracking data, the first 5 points of the MSD plot were fit to  $MSD(\tau) = 4D\tau^\alpha$  (see Figure S2).

### 3D Numerical Simulation of Aggregate Partitioning between Mother and Bud

Simulations of particle diffusion through a bud neck were performed using a spherical cell model where “mother” and “bud” spheres were separated by a barrier except at the position of the neck opening. The mother and bud diameters were set to 5 and 4.5 μm respectively and the neck diameter was adjusted as described in the text. 80000 particles were distributed randomly in three dimensions within the mother box before the start of the simulation. At each time step of the simulation, particles were moved from their previous position in each dimension by a distance given by a Gaussian random number with standard deviation  $\sqrt{2Dt}$  where  $D$  is the diffusion coefficient and  $t$  is the time step. The diffusion coefficient was set to 0.001 μm<sup>2</sup>/s for consistency with the diffusion coefficient in aged cells and the time step was set to 5 s. This value was chosen because it is small enough to prevent large steps outside of the cell boundary but large enough to allow reasonable simulation time (2000 min). Diffusion steps occurring outside of the spheres



were reflected back into the spheres. The barrier between mother and bud was enforced by reflecting any diffusion steps that crossed the neck and did not land within the cylinder delineated by the neck opening. Images were created from the simulations by creating a  $160 \times 160$  nm pixel square corresponding to each particle that was within  $1.25 \mu\text{m}$  of the middle  $z$  plane of the simulation. 1D probability density functions for particle position were then created using custom written kymograph tools in ImageJ (NIH, Bethesda, MD). For 2D probability density functions, a sum projection of all particles was created.

### Simulation of Random Walk with Confinement and Transport Components

Simulations of random diffusion for alpha value distribution analysis and individual trajectory visualization were performed similarly to those described above. Here particle displacements were restricted to two dimensions for consistency with the projected 2D tracking that was performed experimentally. Experimental trajectories are observed for a variable length of time, either due to loss of tracking or disappearance of the particle. We found that the trajectory length distribution was exponential with an average trajectory length of 9.3 frames. In order to match the experimental noise characteristics, our simulated trajectories had lengths specified by an exponential random number with an average of 9.3 frames. Particle positions were updated at each time point as before, but the time between frames was set to 60 s, and the diffusion coefficient was set to  $0.0005 \mu\text{m}^2/\text{s}$  for similarity with that for heat-induced aggregates. In order to simulate restricted motion (sub-diffusion), 30% of the aggregates were not allowed to diffuse more than  $0.5 \mu\text{m}$  from their starting position. Displacements outside of this region were reflected back into the region. In order to simulate transport (super-diffusion), particles were given a 10% probability of transitioning into a “transport” state at each time point. Once in the transport state, the particles moved along a random vector with a linear speed of  $0.005 \mu\text{m}/\text{s}$  while still diffusing with a 100 fold reduced diffusion coefficient compared to the non-transport species. Once in the transport state particles were given a 25% chance at each time point of transitioning back out of the transport state.

### 1D Analytical Model of Aggregate Partitioning between Mother and Bud

#### Statement of Problem

Dynamics of the aggregates in the yeast cells were considered as a constrained random walk, similar to the episomal DNA motion (Gehlen et al., 2011). Simulations were repeated several hundred thousand times and the result was averaged to obtain the distribution of the particles in a region of prescribed geometry. This approach requires long computations and is justified when applied to the problem with complex geometry. When the geometry is simple enough a simpler approximate approach can be used based on numerical and/or analytical solution of the well-known diffusion equation. This approach is justified in an assumption about well-mixing dynamics, i.e., when the averaging of many random trajectories of small number of particles can be effectively replaced by a distribution of very large number of moving particles.

Consider a problem of aggregates dynamics in the budding yeast cell. The geometry is represented by an union of two intersecting spheres of the radii  $R_1$  of mother cell and  $R_2$  of the bud, where  $R_1 > R_2$ . For simplicity assume that at  $t = 0$  all aggregates concentrated in the mother cell and the bud is free of them, so that the initial aggregates distribution  $C(r, t = 0)$  is uniform in the mother compartment and it is zero in the bud.

The dynamics of the particles density is given by the diffusion equation

$$\frac{\partial C}{\partial t} = D \Delta C, \quad (\text{S1})$$

where  $D$  denotes the diffusion coefficient and  $\Delta$  is the Laplacian second order differential operator that in the Cartesian coordinates reads  $\Delta = \partial^2 / \partial x^2 + \partial^2 / \partial y^2 + \partial^2 / \partial z^2$ . Assume that the mother-bud axis coincides with the  $x$  axis, and the center of the mother compartment is in the origin. The region corresponding to the mother compartment is defined as  $|r| < R_1$ , the corresponding region for the bud compartment reads  $|r - R_{20}| < R_2$ , where  $R_{20} = \{R_1 + R_2 - \varepsilon, 0, 0\}$ ; here the maximal size of the overlapping regions  $\varepsilon$  determines the neck size  $d \approx 4R_1^2 \varepsilon / (R_1 + R_2)$ . The boundary conditions assume no flux of concentration at the cell membrane and reads  $n \cdot \nabla C = 0$ , where  $n$  denotes the normal to the boundary and  $\nabla C$  is the concentration gradient.

#### Reduction to 1D Problem

Analysis of 3D numerical solution leads to reduction of the original problem to the 1D version presented below. The equation (S1) converts into

$$\frac{\partial C}{\partial t} = D \frac{\partial^2 C}{\partial x^2}, \quad (\text{S2})$$

that should be solved in the region  $-R_1 \leq x \leq R_1 + 2R_2 - \varepsilon$  subject to the boundary and initial conditions

$$\left. \frac{\partial C}{\partial x} \right|_{x=-R_1} = \left. \frac{\partial C}{\partial x} \right|_{x=R_1+2R_2-\varepsilon} = 0, \quad (\text{S3})$$

$$\begin{aligned} C(x, 0) &= 1, -R_1 \leq x \leq R_1, \\ C(x, 0) &= 0, R_1 \leq x \leq R_1 + 2R_2 - \varepsilon. \end{aligned} \quad (S4)$$

Redefining the spatial variable  $x \rightarrow x - R_1$  and introducing the parameters  $L_1 = 2R_1$  and  $L_2 = 2R_2 - \varepsilon$  we arrive at the updated boundary and initial conditions

$$\left. \frac{\partial C}{\partial x} \right|_{x=-L_1} = \left. \frac{\partial C}{\partial x} \right|_{x=L_2} = 0, \quad (S5)$$

$$\begin{aligned} C(x, 0) &= 1, -L_1 \leq x \leq 0, \\ C(x, 0) &= 0, 0 \leq x \leq L_2. \end{aligned} \quad (S6)$$

### Analytical Solution in 1D

The problem (S2, S5, S6) is solved using the separation of variables method (Tikhonov and Samarskii, 1990) in which the spatial and temporal dependencies in the solution are separated. As the result the linear partial differential equation (S2) splits into two ordinary linear differential equations.

The solution is written as infinite series

$$C(x, t) = A_0 + \sum_{n=1}^{\infty} A_n \cos \frac{\pi n(x+L_1)}{L_1+L_2} \exp \left( -\frac{\pi^2 n^2 D t}{(L_1+L_2)^2} \right), \quad (S7)$$

where the coefficients  $A_n$  are given by

$$A_0 = \frac{L_1}{L_1+L_2}, \quad A_n = \frac{2}{\pi n} \sin \frac{\pi n L_1}{L_1+L_2}, \quad (n > 0).$$

Qualitative analysis of the solution shows that at large times  $Dt \gg 1$  the contribution of the summation terms in (S7) rapidly goes to zero for  $n > 1$ , so that one can use an approximate solution retaining only the first term in the sum

$$C(x, t) \approx \frac{L_1}{L_1+L_2} + \frac{2}{\pi} \sin \frac{\pi L_1}{L_1+L_2} \cos \frac{\pi(x+L_1)}{L_1+L_2} \exp \left( -\frac{\pi^2 D t}{(L_1+L_2)^2} \right). \quad (S8)$$

A comparison of the first 20 terms in (S7) and the 3D experimental simulation for a bud neck diameter of  $4.25 \mu\text{m}$  is shown in Figure 7C at the 90 min time point. The 3D simulation distribution resembles the 1D analytical solution. A comparison in Figure 7A shows that the  $1.25 \mu\text{m}$  girth constrains diffusion to a great extent. Therefore, the 1D solution overestimates the rate at which particles equilibrate between the mother and bud.

### Retention of Particles in the Mother Compartment

Having the exact (S7) and approximate (S8) solution in analytical form we compute the fraction of particles retained in the mother compartment as a function of time. Using the assumption that 3D distribution  $C(x, y, z, t)$  is approximated by the 1D solution  $C(x, y, z, t) = C(x, t)$  we compute the total number  $N_m$  of particles in the mother as integral

$$N_m(t) = \pi \int_{-L_1}^0 r^2 C(x, t) dx, \quad (S9)$$

where  $r$  denotes the radius of the circular cross section orthogonal to the mother-bud axis at position  $x$ . The square of the radius is found from geometry as  $r^2 = -x(x+L_1)$ . The initial particle number  $N_m(0)$  equals to the mother compartment volume  $N_m(0) = \pi L_1^3/6$ . The fraction  $f$  of the mother retained particles reads  $f(t) = N_m(t)/N_m(0)$  and is computed as

$$f(t) = -\frac{6}{L_1^3} \int_{-L_1}^0 x(x+L_1) C(x, t) dx. \quad (S10)$$

Substitution of the exact solution (S7) into (S9) produces the explicit expression

$$f(t) = \nu + \frac{12}{\pi} \sum_{n=1}^{\infty} \frac{\sin a_n}{n a_n^3} [2 \sin a_n - a_n (1 + \cos a_n)] e^{-a_n^2 D t / L_1^2}, \quad (S11)$$

where the parameter  $a_n$  is defined as  $a_n = n\pi\nu$ , and  $\nu = L_1/(L_1 + L_2)$ .

Retaining the first term in the sum in (S10) we find an approximate solution

$$f(t) = \nu + \frac{12}{\pi^4 \nu^3} \exp\left(-\frac{\pi^2 \nu^2 D t}{L_1^2}\right) \sin \pi \nu \cdot [2 \sin \pi \nu - \pi \nu (1 + \cos \pi \nu)]. \quad (\text{S12})$$

It follows from the solution (S11) that the minimal fraction of the particles in the mother compartment equals to  $f_{\min} = \nu$  and it is reached at equilibration time  $t_*$  roughly estimated as  $t_* = (L_1 + L_2)^2 / (\pi D)$ .

Qualitative analysis of the particle dynamics and retention implies that the particles exchange between the two compartments leads to leveling off the concentration distribution at the characteristic time  $t_*$  inversely proportional to the particles diffusivity and proportional to square of the cell size. The negligible exchange may be assigned to two reasons: initial state is close to the dynamical equilibrium, or the diffusion coefficient is small enough to prevent transfer of aggregates between the compartments.

We analyzed the data on fraction  $f$  dynamics for the WT yeast cells and found the value  $f = 0.8$  at the time scale of 90 min (Figure 7B). The estimate of the diffusion coefficient  $D$  based on the aggregates trajectory analysis gives  $D = 1.0 \cdot 10^{-3} \mu\text{m}^2/\text{s}$ . The characteristic cell size is in the range  $2(R_1 + R_2) = 8 - 10 \mu\text{m}$ . The estimate of complete relaxation time produces  $t_* = 600 \text{ min}$ . This means that the random walk motion does not affect the aggregate distribution between the mother and the bud.

#### SUPPLEMENTAL REFERENCES

Giaever, G., Chu, A.M., Ni, L., Connelly, C., Riles, L., Véronneau, S., Dow, S., Lucau-Danila, A., Anderson, K., André, B., et al. (2002). Functional profiling of the *Saccharomyces cerevisiae* genome. *Nature* 418, 387–391.

Schwille, P., Koriach, J., and Webb, W.W. (1999). Fluorescence correlation spectroscopy with single-molecule sensitivity on cell and model membranes. *Cytometry* 36, 176–182.

Steffen, K.K., MacKay, V.L., Kerr, E.O., Tsuchiya, M., Hu, D., Fox, L.A., Dang, N., Johnston, E.D., Oakes, J.A., Tchao, B.N., et al. (2008). Yeast life span extension by depletion of 60s ribosomal subunits is mediated by Gcn4. *Cell* 133, 292–302.

Tikhonov, A.A., and Samarskii, A.A. (1990). *Equations of Mathematical Physics* (Mineola, NY: Dover Publications).

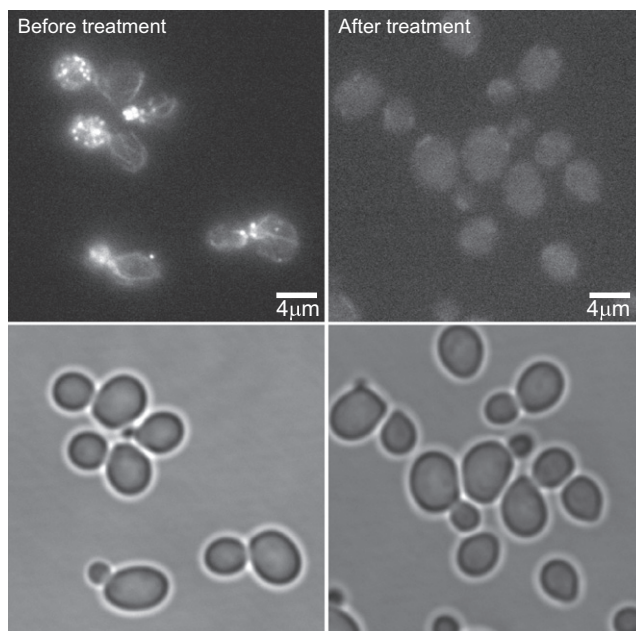


**Figure S1. Analysis of F-Actin Structures in LatA-Treated Cells, Related to Figure 3**

LatA treatment disrupted visible actin structures in wild-type cells. Yeast cells with and without 10 min treatment with 100  $\mu$ M LatA were stained with FITC-phalloidin.



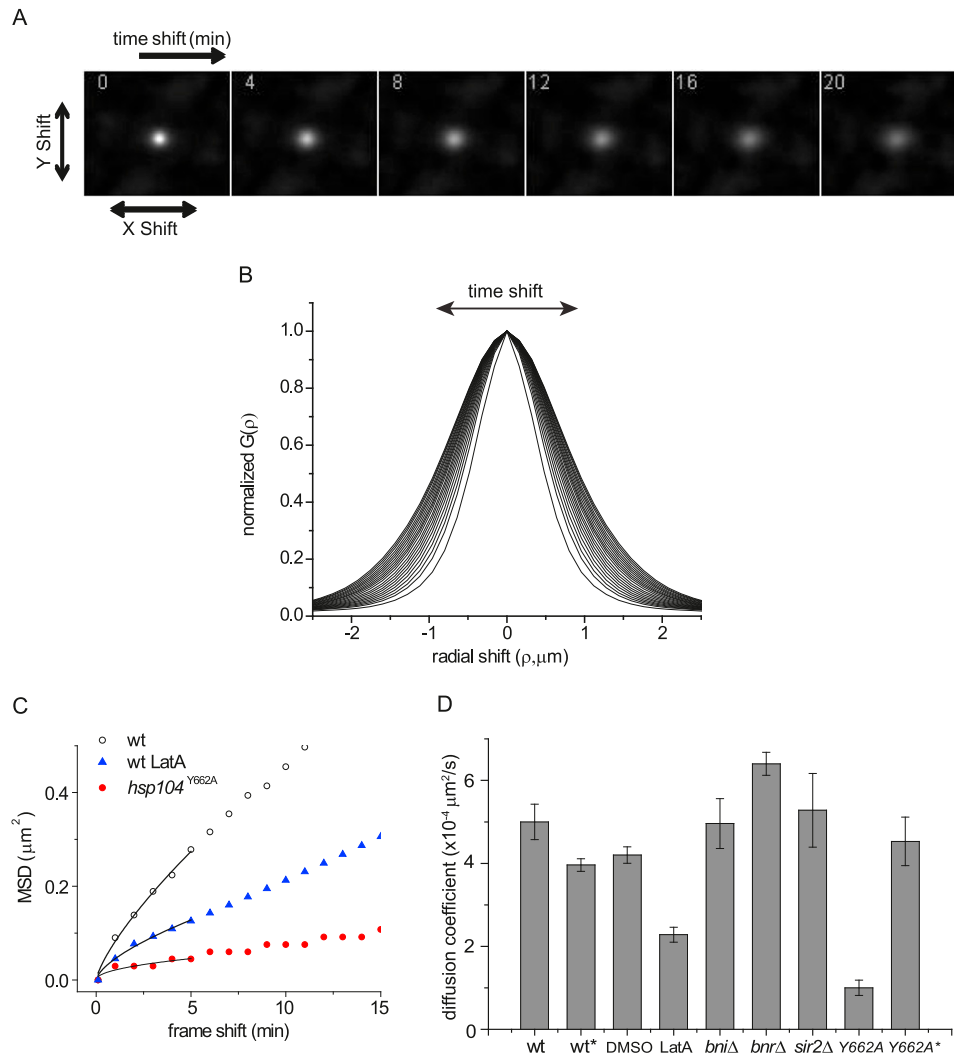


**Figure S2. STICS Analysis of Aggregate Motility, Related to Figure 3**

(A) Following background subtraction (see [Extended Experimental Procedures](#)), the decay of the spatial-temporal correlation function as a function of time shift was calculated. A single value was obtained per field of view of cells. Shown are the spatial correlation related to x and y shift as a function of time shift.

(B) The spatial correlations were circularly averaged to generate plots of  $G(\rho)$  over radial shift. These plots were fit to Gaussians to quantify the increase in width of the spatial-temporal correlation function over time shift, as the motion of the particles decreases the spatial correlation over time. This increase in width was used to calculate MSD for the particles (see [Extended Experimental Procedures](#)). Initial amplitude of  $G(\rho)$  is normalized here to emphasize the increase in width over time shift.

(C) MSD was calculated from the increase in width as shown in (B) (see [Extended Experimental Procedures](#)). Representative MSD plots of STICS results for a single field of view are shown for wild-type (wt), wt + LatA, and  $hsp104^{Y662A}$  (30 min heat shock).

(D) Diffusion coefficients calculated from STICS analysis of different strains and conditions. Y662A\*:  $hsp104^{Y662A}$  mutant with 3.5min heat shock. All other strains and conditions were with 30 min heat shock. Each plot shows the mean and SEM of diffusion coefficient calculated from MSD plots from a minimum of 3 fields of view of cells, with each field of view consisting of 20 to 40 cells.